

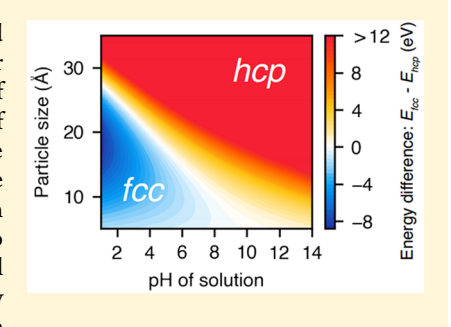
Cite This: J. Am. Chem. Soc. 2018, 140, 17290–17296

Guiding Synthesis of Polymorphs of Materials Using Nanometric Phase Diagrams

Xuetian Ma,[†] Adelaide M. Nolan,[‡] Shuo Zhang,[‡] Jianming Bai,[§] Wenqian Xu,[†] Lijun Wu,^{||} Yifei Mo,*^{,‡}® and Hailong Chen*, To

Supporting Information

ABSTRACT: Conventionally, phase diagrams serve as road maps for the design and synthesis of materials. However, bulk phase diagrams are often not as predictive for the synthesis of nanometric materials, mainly due to the increased significance of surface energy. The change of surface energy can drastically alter the total energy of the nanocrystals and thus yields a polymorph or metastable phase different from the stable phase in bulk, providing a means for controlling the synthesis of metastable phases. To achieve a theoretical and systematical understanding on the polymorphism of nanomaterials, metallic cobalt was chosen as a model system, where the two polymorphs, fcc and hcp phases, can be tuned with 100% selectivity in a solvothermal reaction. Advanced in situ synchrotron X-ray diffraction (XRD) technique and density functional theory (DFT) calculations were complementarily employed to reveal the



size- and surface-dependent polymorphism at nanometer scale. The nanometric phase diagram provides a general predictive approach to guide the synthesis of metastable materials.

■ INTRODUCTION

Nanometric materials, including nanoparticles, nanowires, nanotubes, or other nanostructures, exhibit many interesting physical and chemical properties that differ from those of bulk materials. 1-3 For example, LiFePO₄, a popular cathode material for lithium ion batteries, can only demonstrate ultrahigh rate cycling in nanoparticle form. 4 However, the synthesis of nanometric materials is often very difficult, heavily relying on Edisonian trial-and-error processes⁵ and lacking theoretical and systematical guidelines. At the nanometric scale, many metastable phases and polymorphs may be favored over the thermodynamically stable phase in the phase diagram. Thus, the phase diagrams built upon bulk phase thermodynamics provide limited guidance for synthesizing nanomaterials at the nanometer scale. This deviation from conventional phase diagrams is mainly due to the significant contribution of surface energy into the total energy of the nanometric crystal.6-8 How the surface exactly varies the total energy and thus alters the phase diagram at nanometric scale is the fundamental question necessary for understanding and guiding the synthesis of nanomaterials. In this work, we attempt to address this question by applying ab initio computation on nanoparticles of model materials with different surface conditions in different synthesis environments, and by verifying

the results of experimental synthesis using advanced in situ Xray diffraction techniques.

Previously, many methods have been demonstrated in a wide range of nanomaterials to tune the geometric features, such as the particle size, 9,10 morphology, 11-14 and exposing facets, 15,16 to obtain enhanced properties that are useful for certain applications. The prevailing method to tune the size and morphology of certain functional materials is to use capping agents to control the growth kinetics for the different exposing surfaces. For example, Xia et al. 17 synthesized a cube of silver using polyvinylpyrrolidone (PVP). It is worth noting that most of such works only change the geometric features of the material, but the phase/polymorph of the material remains the same. 18-20 It is rare to see the crystal structure of the material, that is, the symmetry and space group, completely changed depending on the capping status. Some previous investigations did demonstrate that possibility of such dependence. 6-8,21-23 Navrotsky et al. demonstrated experimentally the polymorphs of TiO2, using both adsorbed water molecule and particle size as tuning factors to control the formation of the nanoscale polymorphs (e.g., rutile and anatase). Ceder et al. reported a computational study on

Received: October 12, 2018 Published: November 13, 2018

[†]The Woodruff School of Mechanical Engineering, Georgia Institute of Technology, 771 Ferst Drive, Atlanta, Georgia 30332, United States

^{*}Department of Materials Science and Engineering, University of Maryland, College Park, Maryland 20742, United States

 $^{^{\}S}$ National Synchrotron Light Source II, and $^{\parallel}$ Condensed Matter Physics and Materials Science Department, Brookhaven National Laboratory, Upton, New York 11973, United States

 $^{^{\}perp}$ X-ray Science Division, Advanced Photon Source, Argonne National Laboratory, Argonne, Illinois 60439, United States

calcite mineral using Mg^{2+} as the doping ion to obtain metastable aragonite. In recent research, K^{+8} and Mg^{2+23} were used to tune the formation of different polymorphs of MnO₂ in solution, respectively. However, in the three later cases, the composition of the polymorphs was not exactly the same, due to incorporation of the doping cations. In a parallel effort, we aim to explore the interplay of bulk lattice energy and surface energy in a system with constant composition to reveal and quantitatively evaluate the polymorphism induced solely by surface energy contributions.

For this reason, metallic cobalt was chosen as the model system. Cobalt is known to have two common polymorphs, the hexagonal close-packed (hcp) phase and the face-centered cubic (fcc) phase. In the bulk material, the hcp phase is thermodynamically more stable at lower temperatures, while the fcc phase is more stable above 450 °C. 24 Nanometric Co is widely used as magnetic, electrical, and catalytic materials, warranting the importance of understanding its polymorphism in nanometer scales.²⁵ In previous efforts to synthesize Co nanoparticles, the results varied depending on different synthesis conditions. Some syntheses yield fcc, 26,27 some yield hcp, 28,29 and some yield the mixture of the two. 30 There is a lack of systematic and fundamental understanding as to why these phases selectively form and how to control the selectivity. On the basis of these considerations, we for the first time identified a method that could tune the formation of fcc and hcp Co with 100% selectivity and conducted DFT computations to identify the energy contribution from the surfaces and its critical role in determining the formation of different polymorphs.

MATERIALS AND METHODS

Solvothermal Synthesis. As a typical protocol for the synthesis of Co nanoparticles, 3 mmol of cobalt hydroxide (Co(OH)₂) (99.9%, Alfa Aesar) and a certain amount of potassium hydroxide (KOH) (85%, Alfa Aesar), varying from 0, 1, 2, to 4 g, were dissolved in 12 g of ethylene glycol (EG) (99+%, Alfa Aesar) at room temperature to form solutions with various pH values. The slurry then was transferred into polytretrafluoroethylene (PTFE)-lined 23 mL stainless steel hydrothermal autoclaves (Parr Instrument). The autoclaves were put into an oven at the desired temperature and for the desired reaction time. After the completion of the reaction, the autoclaves were cooled to room temperature. The solid products were separated from the solution by centrifugation at 4000 rpm (Centrifuge, Eppendorf 5804R), washed three times with distilled water and one time with acetone, and finally dried in an oven in air at 60 °C for 2-3 h.

Computational Methods. The ground-state bulk and surface energies of fcc and hcp Co were calculated using density functional theory (DFT) with the projector augmented-wave approach (PAW) as implemented in the Vienna ab initio simulation package (VASP).32 The generalized gradient approximation (GGA) of Perdew-Burke-Ernzerhof (PBE) was used for the exchange-correlation energy.³³ The plane-wave energy cutoff and k-point mesh were consistent with parameters used by the Materials Project (MP).³⁴ Surface calculations were performed using supercells of Co metal slabs with vacuum regions on both sides of the slab. H+, OH-, and H2O adsorbates were added in several locations and concentrations while maintaining the symmetry of the slab surfaces. Surface energies, as dependent on adsorbates and pH, were calculated using the following expression:

$$\gamma = \frac{1}{2A} (E_{\text{slab}} - n_{\text{Co}} E_{\text{bulk}} - n_{\text{ads}} \mu_{\text{ads}})$$

where A is the area of the surface in the slab supercell model, $E_{\rm slab}$ is the total energy of the slab-vacuum supercell, E_{bulk} is the energy of the bulk phase, and μ_{ads} depends on the adsorbate type. For example, for OH⁻ adsorbates, $\mu_{OH} = \Delta G_{H,O}^f + \mu_H^0 + \mu_O^0 + kT \ln(10) \text{pH}.^{35}$ Using the lowest energy configurations for each surface index, the Wulff shapes of Co nanoparticles in different pH conditions were constructed. The Wulff shapes were used to determine the bulk and surface energy of a nanoparticle as dependent on particle size. The total energy was found as a sum of the bulk and surface energy terms. The total energy difference between nanoparticles of each polymorph was calculated to generate the fcc-hcp phase diagram as a function of particle size and pH. The total energies neglected the contribution of the PV term and the entropy term, which are expected to largely cancel out in calculating the energy differences between the two solid

In Situ Synchrotron X-ray Diffraction for the Solvothermal Synthesis. The in situ synchrotron XRD experiments on cobalt nanoparticles were done at beamline X14A (wavelength = 0.7793 Å), the National Synchrotron Light Source (NSLS) at Brookhaven National Laboratory, and at beamline 17-BM-B (wavelength = 0.7277 Å), Advanced Photon Source (APS) at Argonne National Laboratory, with slightly different setups. Co(OH)2, KOH, and EG were mixed to form a pinkish slurry with various pH values with a procedure similar to that described above. An in situ solvothermal cell was used to collect the XRD pattern during the solvothermal reaction, as schematically illustrated in Figure S1. The solution/slurry in the quartz tube with 1 mm inner diameter was heated to the desired temperature with an air blower heater at NSLS and with a ceramic heating cell at APS, respectively.

The temperature of the heating cell was calibrated using a thermal couple placed at the tip of the capillary and using a thermal couple inserted into an empty quartz tube. The calibrations from the two methods have negligible deviations. The quartz tube was spun during heating for the purposes of stirring the solution and averaging the orientations of the powder. XRD patterns were collected with a step size of 10 or 20 °C until the desired temperature was reached. Each XRD scan typically took 5-15 min, depending on the concentration of the solution. At each step, 2 min idling time was used to allow the reaction and temperature to stabilize, and then the temperature was held during the XRD scan. When the desired reaction temperature was reached, such as 200 or 250 °C, the temperature was held for a few hours to allow the reaction fully complete. During this period, XRD scans were taken every 5-30 min, depending on the kinetics of each batch of reaction. Finally, the tube was cooled to room temperature after the scans were done.

Other Characterizations. An X-ray diffractometer (D8 Advanced, Bruker) with molybdenum radiation ($\lambda_{K\alpha 1} = 0.709$ Å) was used to examine the crystalline phase of the synthesized compound from 2θ between 8° and 40° . Rietveld refinement was done to determine the ratio of the polymorphs in the mixture as well as to obtain the lattice parameters using GSAS software.³⁷ High-resolution transmission electron microscopy (HRTEM) and scanning transmission electron microscopy (STEM) were performed to reveal the morphology and crystal structure of as-synthesized Co nanoparticles under various conditions using the double aberration-corrected JEOL-ARM200CF microscope with a cold-field emission gun operated at 200 kV.

RESULTS

Selective Formation of hcp and fcc Co. On the basis of the hypothesis that the surface energy may significantly vary the total energy of nanometric crystals, it would be easiest to observe this effect at the nucleation stage as then the surface atoms take the largest fraction of the total number of atoms. To control the formation of different polymorphs via tuning of surface energy, a natural thought is to use different absorbents/ capping agents. Experimentally, we choose to use a polyolbased solvothermal reduction method to synthesize Co nanoparticles as wet-chemistry synthesis allows more possible capping ions/functional groups, as compared to synthesis with all solid-state reactions or physical metallurgy.³⁸ In the solvothermal synthesis of Co, it turns out that even a very

simple capping agent, OH $^-$, could vary the surface energy enough to change the relative stability of the two polymorphs. In our solvothermal synthesis, Co(OH) $_2$ was used as the cobalt source, while ethylene glycol (EG) was used as both the solvent and the reducing agent, and 0–4 g of KOH was used as the additive. Co(OH) $_2$ is slightly soluble in basic EG solution. The reduction reaction takes place typically at temperature >180 $^{\circ}$ C as follows:

$$Co(OH)_2 \rightarrow Co^{2+} + 2OH^- \tag{1}$$

$$\text{Co}^{2+} + \text{CH}_2\text{OH} - \text{CH}_2\text{OH} \rightarrow \text{Co} + \text{CH}_3\text{COOH} + 2\text{H}^+$$
(2)

With this solution reaction, the newly formed Co⁰ nucleates in very small clusters. Because this reaction requires basic or neutral solution to go forward, as implied in reaction 2, and because metallic Co reacts with acids, therefore, acidic solution was not tested. Table S1 summarizes the synthesis conditions of different samples. Samples obtained from batches with different amounts of KOH (4, 2, 1, and 0 g) are denoted as S1, S2, S3, and S4, respectively. Figure 1 shows the XRD patterns

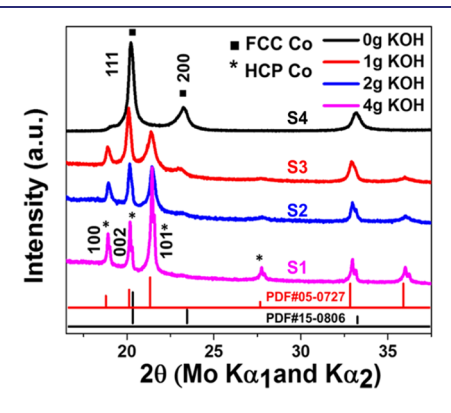


Figure 1. XRD patterns of S1, S2, S3, and S4, synthesized in solvothermal solutions with addition of 4, 2, 1, and 0 g of KOH in 12 g of EG solvent, respectively.

of each sample. For S1, with 4 g of KOH added to obtain a high concentration of OH-, which almost reaches the solubility limit of KOH in EG solvent, the product is pure hcp Co (PDF no. 05-0727). This result is in accordance with the bulk phase diagram in that hcp Co is the stable phase below 450 °C. However, for S4, where no KOH is added and the solution is neutral, the reaction yields a pure fcc Co phase (PDF no. 15-0806). This result clearly deviates from the bulk phase diagram, as the temperature that converts bulk hcp Co to fcc Co is 450 °C, while our reaction temperature is only 200 °C. With an intermediate amount of KOH (1 g) adding in the solution, the product is a mixture of approximately equal amounts of hcp and fcc phases. With increasing amount of KOH to 2 g, sample S2 yields more hcp phase than fcc phase. The relative ratio of the two phases in S2 and S3 phases is extracted by using two-phase whole-pattern fitting on the XRD patterns of these samples. The refinement results and parameters of all four samples are shown in Table S2 and Figure S2. In S2 and S3, the fraction of hcp Co is determined to be 79% and 64%, respectively. This gradual change in the composition of product from pure hcp to the mixture and then to pure fcc shows obvious dependence on the concentration of OH⁻ in the solvothermal solution.

As solvothermal reactions using a statics Parr Instrument vessel without stirring take hours to reach the desired temperature and the reaction is slow and inhomogeneous, it is very difficult to collect samples at the nucleation stage. We collected samples with the shortest reaction time that yields a pure phase for microscopic investigations. Figure 2 shows the

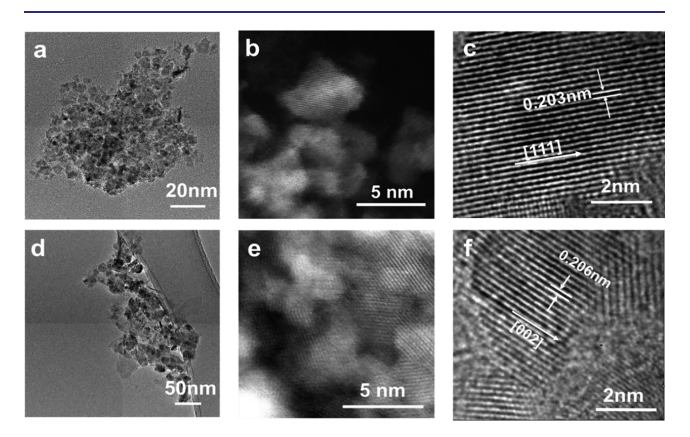


Figure 2. TEM (a,c) and STEM high angle annular dark field (HAADF) (b) images of pure fcc Co nanoparticles, with scale bars of 20, 2, and 5 nm, respectively; and TEM (d,f) and STEM-HAADF (e) images of pure hcp Co nanoparticles, with scale bars of 50, 2, and 5 nm, respectively.

TEM images of Co nanoparticles that yield pure fcc (a-c) and pure hcp (d-f) phases, collected from a 9-h and a 5-h reaction, respectively. The particles show severe agglomeration, but it could be seen that the primary particles are small single crystals with rather uniform sizes. No fused secondary particles were observed. The average size of fcc Co is around 2–4 nm, while for hcp Co it is about 3–5 nm. From the high-resolution images in Figure 2c and f, it could be seen that the particles are well-crystallized. The d-spacing of (111) faces in fcc Co is about 0.203 nm, while the d-spacing between (002) faces in hcp Co is about 0.206 nm, which agree with the values extracted from Rietveld refinement of the XRD patterns. The morphology and the exposing facets of the particles, however, are difficult to clearly identify due to the strong agglomeration of the particles, which is very common for nanoparticles.

Surface Energy of Co Nanoparticles. To understand how surface energy governs the formation of polymorphs of Co nanoparticles, DFT calculations were performed to evaluate the surface structures and surface energy of several low-index facets of fcc and hcp Co phases with various surface adsorbents. According to the Gibbs-Curie-Wulff theorem,³ the shape of a single crystal is a result of minimizing the surface energies of all facets. 40 Calculations were performed for the (100), (110), and (111) surfaces of the fcc phase, and the $(1\overline{1}00)$, (0001), and $(2\overline{1}10)$ surfaces of the hcp phase. The surface energies of surfaces with different adsorbents such as H⁺, OH⁻, and H₂O, with varying surface coverage, were evaluated. The OH- terminated surfaces were found to have the lowest surface energies for all fcc and hcp surfaces over a wide range of pH values (see Figure S3). It should be noted that the acidic pH is only used in computation for the sake of covering a wide range of OH concentrations, while in experiments acidic pH can not be tested because Co reacts with acid to form hydrogen gas.

The calculated surface energies from the lowest-energy surfaces were used to construct Wulff shapes of fcc and hcp Co phases, which show the equilibrium morphology of a particle. Because the calculated surface energy varies with pH (i.e., the concentration of OH⁻), the Wulff shapes also changed as the pH was increased (Figure 3). For all pH levels, the dominant

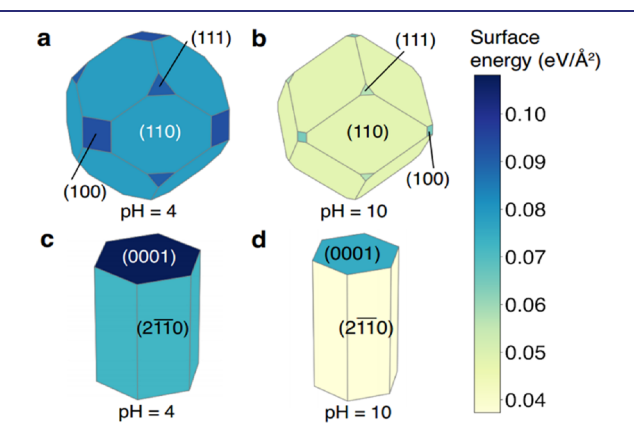


Figure 3. Wulff shapes of fcc Co in acidic condition (a) and basic condition (b); and Wulff shapes of hcp Co in acidic condition (c) and basic condition (d). The color bar indicates the calculated surface energy of each facet.

facet in fcc Co was (110). The energy of the (110) surfaces decreased more rapidly than those of the (111) and (100) facets as the solution became more alkaline (see Figure S3). As a result, with increasing pH, the fraction of the (110) facets in the Wulff shape increased, as shown in Figure 3a and b. The Wulff shape of hcp Co is a hexagonal prism, made of the $(2\overline{110})$ and (0001) facets in all pH conditions (Figure 3c and d). In summary, the surface energies and Wulff shapes of both fcc and hcp Co vary with pH values. This variation impacts the total energies of the Co nanoparticles and their preferences for fcc versus hcp phases as a function of pH (the concentration of OH $^-$ in solution).

Phase Selectivity of Co Nanoparticles. To understand how the thermodynamically favored phase is influenced by the surface energy, the total energy of hcp and fcc Co nanoparticles was calculated and compared to construct a phase diagram as a function of particle size and pH values. The total energy of Co nanoparticles (in both hcp and fcc phases) as a function of particle size was calculated as the sum of the bulk energy and the total surface energy contributed from each facet present (see details in Materials and Methods). The phase diagram with respect to particle size and solution pH was constructed by comparing the total energies of Co nanoparticles in hcp and fcc phases (Figure 4). In short, the pH value determines the morphology of the nuclei and thus also determines the stable polymorph phase in this condition. The total energy difference between the two nanoparticle polymorphs describes the thermodynamic driving force for the formation of a given phase. The larger the energy difference is, the more one phase is favored over the other. As the phase diagram indicates, the fcc phase of Co is favored to nucleate in acidic pH conditions and for smaller particle sizes, while the hcp phase is favored under more basic conditions and favored as the Co particle becomes larger. These calculations could therefore explain the observed formation of hcp Co under high pH and formation of fcc Co under neutral pH at nanometer scale as the result of surface energy contribution. The formation of a mixture of hcp and fcc Co in samples S2 and S3 can be explained because at these intermediate pH values,

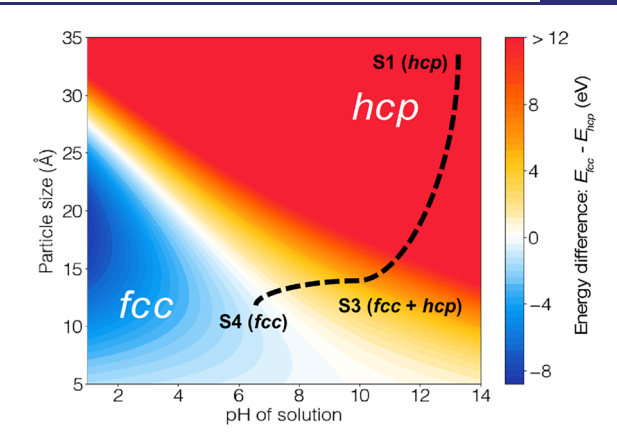


Figure 4. Phase diagram of fcc versus hcp Co nanoparticles with respect to varying particle size and pH level of the solution. The color bar shows the energy differences between the nanoparticles of the two phases. The black dashed line demonstrates the phase composition and particle size observed from the in situ XRD experiments.

the total energies of hcp and fcc nanoparticles are very similar. Therefore, the thermal fluctuations allow for the nucleation of both phases, but with statistical probabilities that are determined by the differences in their total energy (i.e., more hcp phase yields in S2 than in S3 due to the higher pH).

In Situ XRD Investigation. By far, we have demonstrated that the ex situ experiments and computations agree with each other well on the observations that a high concentration of OH⁻ coverage on the surface of the nuclei lowers the energy of the hcp phase as the stable polymorph. However, one could argue that what computation captures is the energy of the nuclei or the nanoclusters with size of a few nanometers, while the XRD patterns, as well as the TEM images, were taken from samples with a few tens of nanometers or micrometer-sized sample. It is possible that the polymorphs may convert during the reaction; therefore, the initial and final phases are different. As it is rather slow to heat and cool the solvothermal reactor, it is impossible to rule out such transformations with post mortem or ex situ observations. Therefore, in situ observation and characterization is essentially necessary. One outstanding challenge is that solvothermal synthesis, and similar hydrothermal synthesis, is previously considered as a black box. Because of the high pressure generated by the solution at elevated temperatures (room temperature to a few hundreds of Celsius), conventionally the solvothermal/hydrothermal reactions have to be carried out in thick-walled press vessels made of high strength metals, which made it impossible to detect the reaction inside in real time with any characterization tools. One can only guess the reactions inside by varying the starting materials and analyzing the products. In this study, we developed a unique platform that allowed us to in situ track the solvothermal reaction with high transmitting synchrotron Xray, as elaborated in Materials and Methods. We were able to track the full path of this solvothermal reaction in real time from starting materials to the nucleation state and the following crystal growth and ripening processes.

Solutions with the same starting materials as those used in the lab synthesis were used in the in situ XRD observations in the sealed quartz tube, S4, S3, and S1, as previously denoted (see Table S3). Figure 5a-c shows the results of in situ solvothermal reactions done at beamline X14A at the National Synchrotron Light Source (NSLS) and at 17-BM-B at the Advanced Photon Source (APS). The reaction starts from

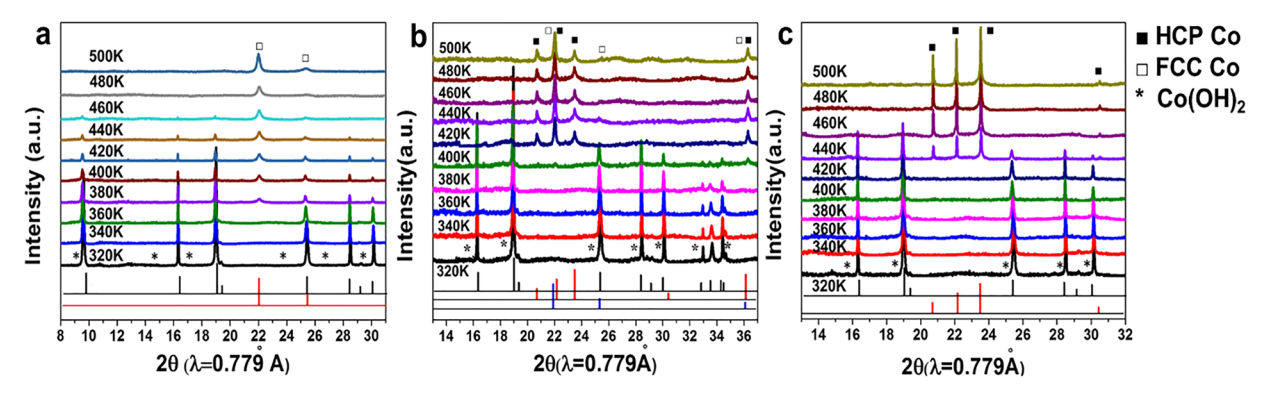


Figure 5. (a) In situ XRD patterns of S4 without KOH addition, (b) S3 with 1 g of KOH addition, and (c) S1 with 4 g of KOH addition in 12 g of EG solvent.

room temperature, with a heating step of 10 °C. As denoted in Figure 5, each reaction starts with Co(OH)2, and gradually shows the nucleation and growth of Co phases while consuming the starting materials. As expected, S4 yields pure fcc Co phase, S3 yields a mixture of hcp and fcc phases, and S1 yields pure hcp Co phase. No phase crossover was observed in any of these experiments, which confirms that the formation of the polymorphs starts directly from nucleation stage. Using the Scherrer equation, the particle size of fcc phase in S4 and hcp phase in S1 and S3 at the nucleation stage is estimated to be around 2, 4, and 3 nm, respectively. The particle size and phase composition of the samples are schematically labeled with the dashed line in Figure 4. Again, it shows that the computation and experiments well agree each other. It should be noted that in experiments, the hcp phase always shows a larger particle size in the in situ XRD observation, either in the pure hcp product or in the hcp—fcc mixed products. It is mainly because the thermodynamic driving force for the formation of hcp phase in high pH environments is greater than that of fcc phase in neutron pH, as indicated by the color in Figure 4. With the greater driving force, the particles of hcp phase grow faster and result in larger size than the fcc phase, under the same heating program in the in situ XRD experiments.

By now, it can be concluded on the basis of both experimental and computational results that the concentration of OH⁻ in solution, or say the pH level of the solution, is a critical factor that influences the stable phase obtained for Co nanoparticles via changing the surface energy by the capping effects of OH-. The hcp Co is more favorable under higher pH conditions, while fcc Co is more stable under neutral condition. This interplay between surface energy and total energy is expected to be general. It would be interesting to see that such surface-controlled polymorphism can be observed with other capping agents other than OH-. Therefore, we designed experiments to use dioctyl sulfosuccinate sodium salt (AOT) (see Figure S4 for the chemical structure of AOT) as an alternative capping agent to observe the polymorphism of Co. In situ solvothermal synthesis using the same Co source (Co(OH)₂) and solvent (EG) but without adding any KOH was carried out on the beamlines. The results, as shown in Figure 6, clearly show that with adding just 1 mmol of AOT, which is a far lower concentration than that of KOH used in previous experiments, the synthesis yields pure hcp Co phase from the nucleation stage. This clearly indicates that AOT has the same capability of varying the surface energy of Co clusters. Because of the selective bonding of AOT ligands with Co facets that lowers the surface energy, it results in an hcp phase

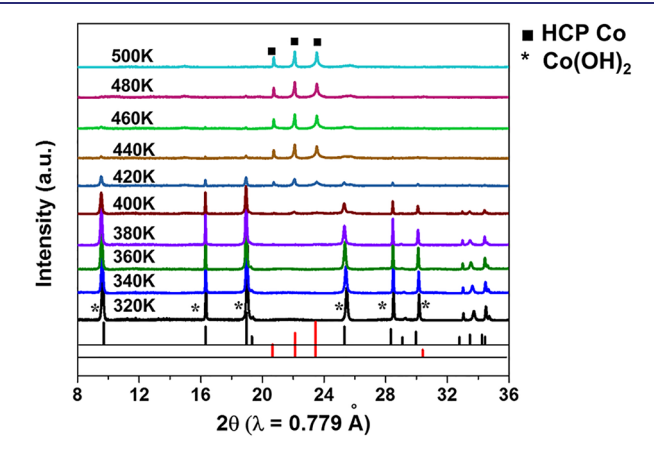


Figure 6. In situ XRD pattern of sample with 1 mmol of AOT addition in 12 g of EG solvent.

formation and growth. This experiment provides another proof of the feasibility and effectiveness of tuning surface energy to vary the total energy and thus tune the polymorphs.

DISCUSSION

In this work, we demonstrate that tuning the surface energy via capping ions can completely change the yielding polymorph for Co nucleation in solution. This tuning of polymorph is purely due to the change of surface energy and does not involve any stoichiometry change as Co is a simple substance, which is different from previous works where such tuning is realized through changes in stoichiometry and composition. This indicates that surface energy by itself could be significant enough to vary the relative stability of different polymorphs. The tuning ability of the surface capping agents depends on both the energetics of the materials as well as the bonding/ adsorption ability of the capping agents. One may expect that, if the difference in bulk energy of the polymorphs is too large, it would be difficult to alter the stable phase by solely changing the surface energy. However, surface energy may become significant as at the nucleation stage the particle size is very small. In this case, the difference between the ground-state energy of the two polymorphs of Co capped with OH- is at the scale of 0.25 kJ/mol⁴¹ (corresponding to the transition temperature of 450 °C), while the surface energy for a 1 nm nucleus under neutral condition (pH = 7), as computed, is 0.76 kJ/mol, which is more than 3 times higher. This implies that this surface energy tuning strategy may be effective for many other materials with even more significantly different

energy among the polymorphs (i.e., higher polymorph crossover temperature in simple heat treatment), considering using capping agents such as AOT with a stronger surface bonding effect than OH-. Polymorphism is very common in many important functional materials, such as TiO₂ (anatase, rutile, brookite), CaCO₃ (calcite, aragonite), and many electrode materials for alkaline metal ion batteries. 42,43 The synthesis of nanometric materials may benefit systematically considering the contribution of surface energy and controlling it accordingly. In fact, we have attempted to tune the polymorphs of alloys. Similar tuning effects can be realized and will be published elsewhere. Such a tuning method in principle can be applied to many more complicated crystalline materials, although the tuning factors may not necessarily be pH or AOT. Other factors such as the solvent or other ligands may be more sensitive and effective.

Another important factor is the bonding ability of the capping agents. When tuning the polymorph of Co with OH-, at least 4 g (or 70 mmol) of KOH was required to form pure hcp phase. However, use of only 0.016 g (1 mmol) of AOT yielded the same pure hcp product in a 12 g EG solution. That is because the bonding between the surface Co atom and OHis relatively weak and very dynamic. A high concentration of OH is necessary to achieve enough coverage that can effectively change the energetics. As a contrast, the SO₃⁻ functional group in AOT has much stronger bonding with surface Co, due to the induction effect of sulfur. 44 Meanwhile, the much higher mass of AOT makes the adsorption much less dynamic and more stable. As a result, a much lower concentration of AOT is needed to yield pure hcp Co. It is also worth noting that the use of capping agent in wetchemistry syntheses is very common for the purpose of tuning the morphology of nanoparticles and nanowires. Yet in those cases, only the growth kinetics was varied due to the selective adsorption of the capping agent on different facets of the material. However, in this case, the formation of different phase-pure polymorphs was governed by thermodynamics, as demonstrated by the computational results and the in situ XRD observation.

More importantly, the nanometric phase diagram with particle size parameter has been established from DFT computation to evaluate and predict the stable phase in nucleation, and is demonstrated with accuracy and effectiveness in the case of Co. In more complicated solutions, more factors such as the competing effect of different ligands and possible stoichiometry change and defects in the crystal need to be considered. As a grand vision, a database of nanometric phase diagrams as the function of particle size, chemical environment, and the concentration of the capping agent can be constructed to guide the synthesis of nanometric polymorphic materials.

CONCLUSIONS

In summary, we combined both experimental results and computational work to generalize an approach to understand the phase selection mechanism of Co polymorphs under solvothermal conditions. It was found that the surface energy was largely affected by the adsorbents, OH⁻, from the solution. In competing with the bulk energy of particles, the surface energy plays an important role in determining the overall energy of the polymorphs for nanometric Co particles, resulting in the formation of various phases under different pH levels. The proposed driving force landscape of fcc and hcp

Co could serve as a reference for selective synthesis of various polymorphs of nanoscale Co for specific applications. This method may be extended to other functional materials besides simple elemental materials, such as alloys, oxides, or carbonates.

ASSOCIATED CONTENT

S Supporting Information

The Supporting Information is available free of charge on the ACS Publications website at DOI: 10.1021/jacs.8b11029.

In situ solvothermal cell setup at X14A at NSLS (Figure S1); synthesis conditions of $Co(OH)_2$ in EG with different KOH amounts (Table S1); Rietveld refinement results and parameters of S1–S4 (Figure S2, Table S2); comparison of surface energy of various low-index facets of hcp and fcc Co with different adsorbents $(OH^-, H^+, and H_2O)$ over a pH range of 0–14 (Figure S3); in situ synthesis conditions of $Co(OH)_2$ in EG with different KOH amounts (Table S3); and chemical structure of AOT (dioctyl sulfosuccinate sodium salt) (Figure S4) (PDF)

AUTHOR INFORMATION

Corresponding Authors

*yfmo@umd.edu

*hailong.chen@me.gatech.edu

ORCID ®

Yifei Mo: 0000-0002-8162-4629 Hailong Chen: 0000-0001-8283-2860

Note:

The authors declare no competing financial interest.

ACKNOWLEDGMENTS

X.M. and H.C. thank the funding support from the National Science Foundation under grant number 1605692 and 1739884, and the faculty start-up fund of Georgia Institute of Technology. A.M.N., S.Z., and Y.M. acknowledge the support from the National Science Foundation under award no. 1550423 and the computational facilities from the University of Maryland supercomputing resources, the Maryland Advanced Research Computing Center (MARCC), and the Extreme Science and Engineering Discovery Environment (XSEDE) supported by National Science Foundation award no. DMR150038. This research used resources of the beamline X14A of the National Synchrotron Light Source, a U.S. Department of Energy (DOE) Office of Science User Facility operated for the DOE Office of Science by Brookhaven National Laboratory under contract no. DE-AC02-98CH10886, and Advanced Photon Source, a U.S. Department of Energy (DOE) Office of Science User Facility operated for the DOE Office of Science by National Laboratory under contract no. DE-AC02-06CH11357. TEM work was supported by the U.S. Department of Energy, Office of Basic Energy Science, Division of Materials Science and Engineering, under contract no. DE-SC0012704.

REFERENCES

- (1) Radtke, G.; Dresselhaus, M.; Chen, G.; Be, V. Size Effects on the Hydrogen Storage Properties of Nanostructured Metal Hydrides: A Review. *Int. J. Energy Res.* **2007**, *31* (6–7), 637–663.
- (2) Leslie-pelecky, D. L.; Rieke, R. D. Magnetic Properties of Nanostructured Materials. *Chem. Mater.* **1996**, 4756 (8), 1770–1783.

- (3) Khlebtsov, N. G.; Dykman, L. A. Optical Properties and Biomedical Applications of Plasmonic Nanoparticles. *J. Quant. Spectrosc. Radiat. Transfer* **2010**, *111* (1), 1–35.
- (4) Malik, R.; Burch, D.; Bazant, M.; Ceder, G. Particle Size Dependence of the Ionic Diffusivity. *Nano Lett.* **2010**, *10* (10), 4123–4127
- (5) Cantisani, A. Technological Innovation Processes Revisited. *Technovation* **2006**, 26 (11), 1294–1301.
- (6) Levchenko, A. A.; Li, G.; Boerio-goates, J.; Woodfield, B. F.; Navrotsky, A. TiO₂ Stability Landscape: Polymorphism, Surface Energy, and Bound Water Energetics. *Chem. Mater.* **2006**, *84* (4), 6324–6332.
- (7) Sun, W.; Jayaraman, S.; Sun, W.; Jayaraman, S.; Chen, W.; Persson, K. A.; Ceder, G. Nucleation of Metastable Aragonite CaCO₃ in Seawater. *Proc. Natl. Acad. Sci. U. S. A.* **2015**, *112* (11), 3199–3204.
- (8) Chen, B. R.; Sun, W.; Kitchaev, D. A.; Mangum, J. S.; Thampy, V.; Garten, L. M.; Ginley, D. S.; Gorman, B. P.; Stone, K. H.; Ceder, G.; Toney, M. F. Understanding Crystallization Pathways Leading to Manganese Oxide Polymorph Formation. *Nat. Commun.* **2018**, *9* (1), 2553
- (9) Chan, E. M.; Mathies, R. A.; Alivisatos, A. P.; Di, V.; Berkeley, L. Size-Controlled Growth of CdSe Nanocrystals in Microfluidic Reactors. *Nano Lett.* **2003**, 3 (2), 1–3.
- (10) Sun, S.; Zeng, H. Size-Controlled Synthesis of Magnetite Nanoparticles. J. Am. Chem. Soc. 2002, 124 (28), 8204-8205.
- (11) Wiley, B.; Sun, Y. Synthesis of Silver Nanostructures with Controlled Shapes and Properties. *Acc. Chem. Res.* **2007**, *40* (10), 1067–1076.
- (12) Peng, X.; Manna, L.; Yang, W.; Wickham, J.; Scher, E.; Kadavanich, A.; Alivisatos, A. P. Shape Control of CdSe Nanocrystals. *Nature* **2000**, 404 (6773), 59–61.
- (13) Chen, H.; Wu, L.; Zhang, L.; Zhu, Y.; Grey, C. P. LiCoO₂ Concaved Cuboctahedrons from Symmetry-Controlled. *J. Am. Chem. Soc.* **2011**, *133* (2), 262–270.
- (14) Lu, Z.; Chen, H.; Robert, R.; Zhu, B. Y.; Deng, J.; Wu, L.; Chung, C. Y.; Grey, C. P. Citric Acid- and Ammonium-Mediated Morphological Transformations of Olivine LiFePO₄ Particles. *Chem. Mater.* **2011**, 23 (11), 2848–2859.
- (15) Han, X.; Jin, M.; Xie, S.; Kuang, Q.; Jiang, Z.; Jiang, Y.; Xie, Z.; Zheng, L. Synthesis of Tin Dioxide Octahedral Nanoparticles with Exposed High-Energy {221} Facets and Enhanced Gas-Sensing Properties. *Angew. Chem., Int. Ed.* **2009**, *48* (48), 9180–9183.
- (16) Chen, H.; Grey, C. P. Molten Salt Synthesis and High Rate Performance of the "Desert-Rose Form" of LiCoO₂. *Adv. Mater.* **2008**, 2 (110), 2206–2210.
- (17) Sun, Y.; Xia, Y. Shape-Controlled Synthesis of Gold and Silver Nanoparticles. *Science* **2002**, 298 (5601), 2176–2179.
- (18) Mehra, R. K.; Yang, Y.; Risbud, S. H. Synthesis, Optical Spectroscopy and Ultrafast Electron Dynamics of PbS Nanoparticles with Different Surface Capping. *J. Phys. Chem. B* **2000**, *104* (49), 11598–11605.
- (19) Catherine J, Murphy. Nanocubes and Nanoboxes. *Science* **2002**, 298 (5601), 2139–2141.
- (20) Zeng, J.; Zheng, Y.; Rycenga, M.; Tao, J.; Li, Z.; Zhang, Q.; Zhu, Y. Controlling the Shapes of Silver Nanocrystals with Different Capping Agents. J. Am. Chem. Soc. 2010, 132 (25), 8552–8553.
- (21) Kitchaev, D. A.; Ceder, G. Evaluating Structure Selection in the Hydrothermal Growth of FeS2 Pyrite and Marcasite. *Nat. Commun.* **2016**, *7*, 13799.
- (22) Kitchaev, D. A.; Dacek, S. T.; Sun, W.; Ceder, G. Thermodynamics of Phase Selection in $\rm MnO_2$ Framework Structures through Alkali Intercalation and Hydration. *J. Am. Chem. Soc.* **2017**, 139 (7), 2672–2681.
- (23) Hu, X.; Kitchaev, D. A.; Wu, L.; Zhang, B.; Meng, Q.; Poyraz, A. S.; Marschilok, A. C.; Takeuchi, E. S.; Takeuchi, K. J.; Ceder, G.; Zhu, Y. Revealing and Rationalizing the Rich Polytypism of Todorokite MnO₂. *J. Am. Chem. Soc.* **2018**, *140* (22), 6961–6968.
- (24) Erbudak, M.; Wetli, E.; Hochstrasser, M.; Pescia, D.; Vvedensky, D. D. Surface Phase Transitions during Martensitic

- Transformations of Single-Crystal Co. Phys. Rev. Lett. 1997, 79 (10), 1893–1896.
- (25) Lu, A. H.; Salabas, E. L.; Schüth, F. Magnetic Nanoparticles: Synthesis, Protection, Functionalization, and Application. *Angew. Chem., Int. Ed.* **2007**, *46* (8), 1222–1244.
- (26) Song, Y.; Modrow, H.; Henry, L. L.; Saw, C. K.; Doomes, E. E.; Palshin, V.; Hormes, J.; Kumar, C. S. Microfluidic Synthesis of Cobalt Nanoparticles. *Chem. Mater.* **2006**, *18* (12), 2817–2827.
- (27) Grass, R. N.; Stark, W. J. Gas Phase Synthesis of fcc-Cobalt Nanoparticles. J. Mater. Chem. 2006, 16 (19), 1825–1830.
- (28) Diana, S.; Lee, S.; Petroff, P. M.; Kramer, E. J. Fabrication of hcp-Co Nanocrystals via Rapid Pyrolysis in Inverse PS-B-PVP Micelles and Thermal Annealing. *Nano Lett.* **2003**, *3* (7), 891–895.
- (29) Puntes, V. F.; Zanchet, D.; Erdonmez, C. K.; Alivisatos, A. P. Synthesis of hcp-Co Nanodisks. *J. Am. Chem. Soc.* **2002**, *124* (43), 12874–12880.
- (30) Guo, F.; Zheng, H.; Yang, Z.; Qian, Y. Synthesis of Cobalt Nanoparticles in Ethanol Hydrazine Alkaline System (EHAS) at Room Temperature. *Mater. Lett.* **2002**, *56* (6), 906–909.
- (31) Joubert, D. From Ultrasoft Pseudopotentials to the Projector Augmented-Wave Method. *Phys. Rev. B: Condens. Matter Mater. Phys.* 1999, 59 (3), 1758–1775.
- (32) Kresse, G.; Furthmüller, J. Efficient Iterative Schemes for Ab Initio Total-Energy Calculations Using a Plane-Wave Basis Set. *Phys. Rev. B: Condens. Matter Mater. Phys.* **1996**, 54 (16), 11169–11186.
- (33) Perdew, J. P.; Burke, K.; Ernzerhof, M. Generalized Gradient Approximation Made Simple. *Phys. Rev. Lett.* **1996**, 77 (18), 3865–3868
- (34) Jain, A.; Hautier, G.; Moore, C. J.; Ping Ong, S.; Fischer, C. C.; Mueller, T.; Persson, K. A.; Ceder, G. A High-Throughput Infrastructure for Density Functional Theory Calculations. *Comput. Mater. Sci.* **2011**, *50* (8), 2295–2310.
- (35) Sun, R. Photovoltaic Properties and Size-pH Phase Stability of Iron Disulfide from Density-Functional Theory. Ph.D. Thesis, Massachusetts Institute of Technology, 2013.
- (36) Ong, S. P.; Wang, L.; Kang, B.; Ceder, G. Li-Fe-P-O₂ Phase Diagram from First Principles Calculations. *Chem. Mater.* **2008**, 77 (4), 1798–1807.
- (37) Toby, B. H. EXPGUI, a Graphical User Interface for GSAS. J. Appl. Crystallogr. 2001, 34 (2), 210–213.
- (38) Feldmann, B. C. Polyol-Mediated Synthesis of Nanoscale Functional Materials. *Adv. Funct. Mater.* **2003**, *13* (2), 101–107.
- (39) Li, R.; Zhang, X.; Dong, H.; Li, Q.; Shuai, Z.; Hu, W. Gibbs Curie Wulff Theorem in Organic Materials: A Case Study on the Relationship between Surface Energy and Crystal Growth. *Adv. Mater.* **2016**, 28 (8), 1697—1702.
- (40) Hwee, C.; Ng, B.; Fan, W. Y. Shape Evolution of Cu_2O Nanostructures via Kinetic and Thermodynamic Controlled Growth. J. Phys. Chem. B **2006**, 110 (42), 20801–20807.
- (41) Kitakami, O.; Sato, H.; Shimada, Y.; Sato, F.; Tanaka, M. Size Effect on the Crystal Phase of Cobalt Fine Particles Osamu. *Phys. Rev. B: Condens. Matter Mater. Phys.* **1997**, *56* (21), 849–854.
- (42) Shinichi, S.; Chem, P.; Phys, C. Negative Electrodes for Na-Ion Batteries. *Phys. Chem. Chem. Phys.* **2014**, *16* (29), 15007.
- (43) Wang, L. P.; Yu, L.; Wang, X.; Xu, Z. J. Recent Developments in Electrode Materials for Sodium-Ion Batteries. *J. Mater. Chem. A* **2015**, *3* (18), 9353–9378.
- (44) Jin, T.; Yamaguchi, T.; Tanabe, K. Mechanism of Acidity Generation on Sulfur-Promoted Metal Oxides. *J. Phys. Chem.* **1986**, *90* (20), 4794–4796.